RESEARCH ARTICLE

Key Points:
- Convective self-aggregation weakens with increased CCN concentration
- Precipitation decrease follows from weakened convective self-aggregation
- Precipitation response scales with the mean radiative cooling and the area-weighted radiatively driven subsidence velocity

Supporting Information:
- Supporting Information S1

Correspondence to:
H. Beydoun,
hassan.beydoun@kit.edu

Aerosol-Cloud-Precipitation Interactions in the Context of Convective Self-Aggregation

H. Beydoun[1] and C. Hoose[1]

[1]Institute for Meteorology and Climate Research, Karlsruhe Institute of Technology, Karlsruhe, Germany

Abstract We investigate the sensitivity of self-aggregated radiative-convective-equilibrium cloud-resolving model simulations to the cloud condensation nuclei (CCN) concentration. Experiments were conducted on a long (2,000-km × 120-km) channel domain, allowing the emergence of multiple convective clusters and dry regions of subsidence. Increasing the CCN concentration leads to increased moisture in the dry regions, increased midlevel and upper level clouds, decreased radiative cooling, and decreased precipitation. We find that these trends follow from a decrease in the strength of the self-aggregation as measured by the moist static energy (MSE) variance. In our simulations, precipitation is correlated, both locally and in total, with the distribution of MSE anomalies. We thus quantify changes in the adiabatic/diabatic contributions to MSE anomalies (Wing & Emanuel, 2014, https://doi.org/10.1002/2013MS000269) and relate those changes to changes in precipitation. Through a simple two-column conceptual model, we argue that the reduction in precipitation can be explained thermodynamically by the reduction in mean net radiative cooling and mechanistically by the weakening of the area-weighted radiatively driven subsidence velocity—defined as the ratio of the total radiative cooling over the dry regions and the static stability. We interpret the system's response to increasing CCN as a thermodynamically constrained realization of an aerosol indirect effect on clouds and precipitation.

1. Introduction

The tropical atmosphere relies on deep convection to vertically transport heat and moisture and consequently drive the tropical circulation (Manabe & Strickler, 2002; Randall, 2015; Riehl & Malkus, 1958). For decades now, researchers have turned to the radiative-convective-equilibrium (RCE) paradigm to comprehend the complex interactions between convective transport, radiative cooling, and the circulations that ensue. On long enough time scales, the assumption of a balance between convective transport of surface fluxes and net radiative cooling in the tropical atmosphere is valid, deeming the approach quite insightful (e.g., Held et al., 1993; Stephens et al., 2008; Tompkins & Craig, 1998; Wing & Cronin, 2016).

Tropical deep convection takes on organized forms that span a range of spatial and temporal scales (Houze, 2004). A particularly interesting form of organization that can take place in cloud-resolving models run to RCE is convective self-aggregation, in which convection clusters into a single or multiple regions of the domain despite initially homogenous conditions (Bretherton et al., 2005). The rest of the domain experiences significant drying and thus increased radiative cooling at model top. Self-aggregated atmospheres are on average drier and rainier than their nonaggregated counterparts, with moisture concentrated in the convectively active and accordingly strongly precipitating regions. While the real tropical atmosphere does not self-aggregate in this particular fashion, recent observations suggest that tropical convection does exhibit some form of aggregation with similar profiles of water vapor, turbulent surface fluxes, and radiation to what is being produced by self-aggregated numerical simulations at RCE (Holloway et al., 2017; Stein et al., 2017; Tobin et al., 2012). As it is currently far too computationally expensive to numerically resolve convection along with the global circulation in which it is embedded (and interacts with), cloud system resolving numerical simulations of self-aggregated RCE are a promising compromise.

The challenge in modeling clouds at all relevant scales is a leading contributor to the long standing problem of whether aerosol particles can exert an influence on cloud physics (Boucher et al., 2013). The solution to the aerosol-cloud problem thus partially hinges on properly simulating clouds on large and long enough scales to ascertain how the aerosol effects manifest (see Fan et al., 2016, for a comprehensive review on aerosol-cloud interactions). Therefore, as we turn to cloud-resolving simulations at RCE to gain a better understanding of how clouds interact with their environment, we can simultaneously gain a better
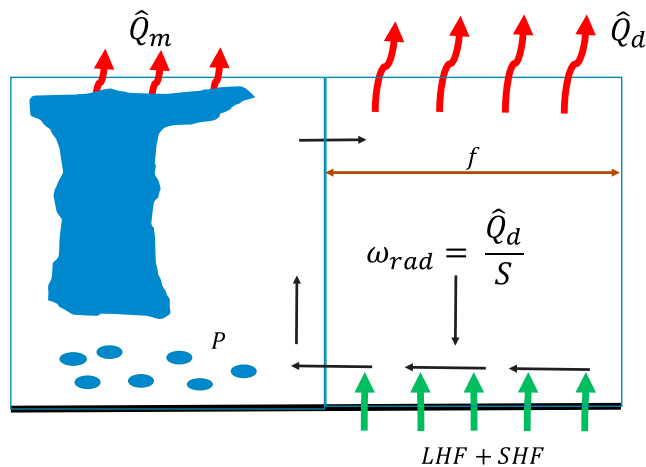
Figure 1. Schematic of the two-box model. Left-hand side is the moist region and the right-hand side is the dry region. *LHF* = latent heat flux; *SHF* = sensible heat flux.

understanding of the role of (perturbed) cloud microphysics in shaping the interactive cloud field. This is not the first effort at investigating aerosol-cloud interactions in an RCE framework. Grabowski (2006), Grabowski and Morrison (2011), van den Heever et al. (2011), Storer and van den Heever (2013), and Khairoutdinov and Yang (2013) are all notable studies. Of these, only van den Heever et al. (2011) and the follow-up work of Storer and van den Heever (2013) dealt with simulations that self-aggregated. Their simulations were carried out on a 10,000-km-long two-dimensional domain in which the cloud condensation nuclei (CCN) concentration was varied. It was found that the RCE state was only slightly sensitive to the changes in the CCN, but notable changes were incurred on the trimodal cloud distribution (specifically, increases in high and midlevel clouds at the expense of low level clouds with increasing CCN). This pointed to compensating feedbacks that rendered the large scale effect small. With the quantitative advents made in analyzing self-aggregation in RCE in the last few years, we think it is a worthwhile endeavor to revisit these experiments and quantify the feedbacks that arise when CCN concentrations are changed. In doing so, not only do we aid in building a more coherent theory of aerosol-deep convection interactions but we also gain insight into the sensitivity of the aggregated RCE state to the cloud microphysics. Our research question is thus: How does the microphysical perturbation of impeding cloud to rain conversion through increasing the CCN concentration translate to the large-scale state as measured by the strength of the convective self-aggregation and the RCE energy balance? And if the large-scale state is buffered, how do the contributing adiabatic and diabatic mechanisms achieve this buffering? We will focus only on aerosol perturbations through impacts on CCN. This is a limitation since changes in the aerosol concentration in the real atmosphere bring direct effects on radiation that act in conjunction with the indirect effect on clouds. However, this more comprehensive treatment is beyond the scope of this work. Furthermore, since our focus is on the large-scale RCE state, our analysis will mostly be confined to the effects of cloud drop number changes on the energetics and self-aggregation of our simulations and not the detailed microphysical pathways through which these changes occur.

The paper is structured as follows: Section 2 discusses a conceptual model of our research question, section 3 describes the model setup, section 4 gives an overview of the RCE state reached by the simulations, section 5 discusses the results in terms of a moist static energy (MSE) budgeting framework (Wing & Emanuel, 2014), section 6 investigates the overturning circulation, and section 7 concludes the paper.

2. A Two-Column Model for Conceptualizing Aerosol-Cloud Interactions in Aggregated RCE

An impact of an increase in cloud drop number concentration on the energy balance and overturning circulation of a self-aggregated atmosphere in RCE must satisfy thermodynamic constraints. In this section, we will examine whether such an impact is conceivable.

Figure 1 presents a two-column model conceptualizing the energy balance achieved by self-aggregated atmospheres at RCE. The left hand side is characterized by low level convergence of moist air, convection, and high cloud and moisture contents. The right side is characterized by upper level divergence, dryness, and radiatively driven large-scale subsidence that is thermodynamically constrained by (Randall, 2015)

$$\omega_{rad} = \frac{\hat{Q}_d}{S}. \tag{1}$$

In equation (1), ω_{rad} is the radiatively driven subsidence pressure velocity (Pa/day), $\hat{Q}_d$ is the net (top of atmosphere—surface) radiative cooling rate in the dry column (K/day) where the ^ symbol is used to denote a column integrated variable, and S is the dry static stability $\frac{T}{\theta}\frac{d\theta}{dp}$ (K/Pa) where θ is the potential temperature and p is the atmospheric pressure. S is the same in the both columns due to the applicability of the weak

temperature gradient approximation (e.g., Sobel et al., 2001). The two-column model temperature and cloud amount are conceptualized to be height dependent while the subsidence and updraft velocities are conceptualized to be constant in height. Although S varies with height for a temperature profile resembling a moist adiabat, here we assume S to be a single mean representative stability of the entire column.

At RCE, surface heat fluxes exactly balance the net (top of atmosphere—surface) radiative cooling of the atmosphere:

$$LHF + SHF = f\widehat{Q}_d + (1-f)\widehat{Q}_m = \widehat{Q}_{net},\qquad(2)$$

where LHF is the surface latent heat flux, SHF is the surface sensible heat flux, $\widehat{Q}_m$ is the radiative cooling rate in the dry column, and f is the areal fraction of the domain covered by subsidence.

Since surface precipitation must balance the surface latent heat flux and SHF is small compared to LHF over a constant temperature sea surface (e.g., Tompkins & Craig, 1998), we expect that precipitation scales (change proportionally) with the mean net radiative cooling:

$$P\sim\widehat{Q}_{net},\qquad(3)$$

where P is the surface precipitation. Equation (3) represents a first scaling relation for the surface precipitation. A second scaling relation for precipitation can be hypothesized using the constraint on subsidence stated in equation (1). If mean precipitation scales with mean ascent then by continuity P would scale with the area-weighted subsidence velocity (e.g., Albern et al., 2018):

$$P\sim f\omega_{rad}.\qquad(4)$$

The moisture content of near surface updrafts is constrained by the water vapor saturation pressure at the temperature of the underlying surface (a Clausius-Clapeyron constraint). Hence, the validity of equation (4) is contingent on the assumption of a constant sea surface temperature, which is the case here.

Higher cloud droplet number concentrations (achieved through increasing the CCN concentration) can hinder the conversion of suspended condensate to rain drops resulting in a cloudier moist column and thus a lower $\widehat{Q}_m$—assuming the cloud increase is more substantial at high altitudes. The reduced cooling can then increase column stability, S. In this hypothetical response, P would decrease by equation (3) while equation (4) would stipulate the hypothesized mechanism by which this decrease in precipitation is achieved: a weakening in the overturning circulation and thus a decrease in the moist region's mean ascent. Additionally, since self-aggregated atmospheres are characterized by substantial contrasts in the column moisture budgets between the moist and dry regions, the weakening of the overturning circulation may result in the weakening of the self-aggregated state. Such a response would be consistent with the fact that self-aggregated atmospheres exhibit higher radiative cooling and thus higher precipitation rates than their nonaggregated counterparts (e.g., Wing et al., 2017). Weaker self-aggregation may also decrease f (Cronin & Wing, 2017) exacerbating the precipitation decrease deduced from equations (3) and (4). We can therefore conclude that, at least conceptually, there are energetically consistent pathways through which cloud microscale assumptions can protrude onto the large-scale state.

Our simulations will be validated against the well-established equation (3) (Riehl & Malkus, 1958) in section 4. We will quantify whether changes in self-aggregation accompany changes in the energy balance in section 5. We will then examine changes in the circulation and the validity of equation (4) in section 6.

3. RCE Cloud-Resolving Model Simulations With ICON-LEM

We conduct simulations with the ICOsahedral nonhydrostatic large eddy model (ICON-LEM; Dipankar et al., 2015) on an elongated 3-D channel domain with periodic boundary conditions. The ICON model solves the fully three-dimensional nonhydrostatic and compressible Navier-Stokes on triangular grids (Heinze et al., 2017; Zängl et al., 2015). The simulations here all use edge lengths of 3 km, yielding an effective grid spacing of just under 2 km (1.95 km). The total number of grids in the horizontal is $1{,}000 \times 60$, which results in a channel domain with horizontal dimensions of about 2,000 km by 120 km. There are

72 vertical levels, which increase in spacing from 35 m in the first level to 500 m near the top. The vertical dimension of the domain is 28 km. Classical Rayleigh damping is applied from 19.5 km upward to prevent gravity wave reflection and build up.

For model physics, we use classical Smagorinsky diffusion (Lilly, 1962) and an updated version of the two moment cloud microphysics scheme of Seifert and Beheng (2006). The two moment scheme predicts the number and mass mixing ratios of two liquid (cloud and rain) and four frozen (ice, graupel, snow, and hail) hydrometeor categories. Convection is not parameterized. As with previous studies of RCE in CRMs, there is no diurnal cycle with the zenith angle and solar insolation fixed at 42.05° and 551.58 W/m^2, respectively. The SST is prescribed at 300 K and there is no rotation. For radiation, we use the Rapid Radiation Transfer Model (Mlawer et al., 1997). The surface turbulent fluxes are computed interactively using Monin-Obukhov similarity theory.

Simulations are initialized with the analytical sounding from Reed and Jablonowski (2011) which approximates the moist tropical sounding from Dunion (2011). Horizontal winds are initially set to zero and the domain wide mean wind is relaxed to zero on a time scale of 3 hr throughout the course of the simulations. Without the relaxation, flows reminiscent of the quasi-biennial oscillation of the simulations from Held et al. (1993) develop and cause strong fluctuations in the strength of the aggregation. For our simulations we found that the model output was significantly less noisy and thus easier to analyze with this relaxation. The condition is on the mean wind, thus local winds are allowed to evolve which is necessary for the formation of the aggregated state and the associated overturning circulations. The vertical velocity and virtual potential temperature fields are initialized with random noise on the order of 0.05 m/s and 0.2 K, respectively, in the three lowest model levels. This was done to break the symmetry and initialize convection within the first few hours of start of the simulations.

The paper deals with five simulations with the same model configuration except for the CCN concentration. The CCN concentration is parameterized following Hande et al. (2016), where the number concentration of activated cloud droplets is predicted from the pressure and vertical velocity:

$$CCN(w, p) = E_{CCN} CCN_{default}(w, p). \tag{5}$$

E_{CCN} is a free parameter that we have introduced to scale the Hande et al. (2016) parameterization to a desired CCN concentration. At 900 hPa, $CCN_{default}$ results in CCN concentrations of 600 and 1,100 cm^{-3} for updraft speeds of 0.5 and 5 m/s, respectively. At 500 hPa, the concentrations drop to about 60 and 110 cm^{-3}. We thus consider this configuration as the "intermediate" case and use values of 0.05, 0.2, 5, and 10 for E_{CCN} to simulate cases "very low" (30 cm^{-3}), "low" (120 cm^{-3}), "high" (3,000 cm^{-3}), and "very high" (6,000 cm^{-3}). The two highest CCN concentrations are exaggerated on purpose, so as to represent bounds on the variability of the system's response to CCN concentrations. The reader is referred to the original publication of Hande et al. (2016) for information for how to compute $CCN_{default}$ and supporting information Figure S1 for vertical profiles for the five CCN cases.

Introduced by Bretherton et al. (2005), mesoscale block averaging by column relative humidity (CRH) is a very useful tool for analyzing self-aggregated CRMs run to RCE. CRH, as in Bretherton et al. (2005) and Wing and Cronin (2016), is defined as the ratio of column integrated water vapor path and column integrated saturation water vapor path. In this work we employ two types of block averaging. The first type is similar to what has been done in previous studies, whereby the domain is first partitioned into a certain number of blocks (one hundred 20-km × 120-km blocks for our default simulations) then ranked by CRH. The second type ranks individual grid cells by CRH first then averages the properties of an equal number of grids for 150 CRH values from highest to lowest. We find that the latter approach gives insights into the convective core that the former approach averages out. We will indicate which two block averaging method is employed when discussing our results.

The choice of domain size and geometry was a compromise between a domain size large enough to result in multiple convective regions but small enough to suit our computational resources. This domain is 6 to 9 times smaller than the long channel domain used in previous studies employing this geometry (Stephens et al., 2008; Wing & Cronin, 2016), but we do use a higher resolution (2 km as opposed to 3 km) and employ the more computationally expensive two moment microphysics scheme. Previous studies have investigated
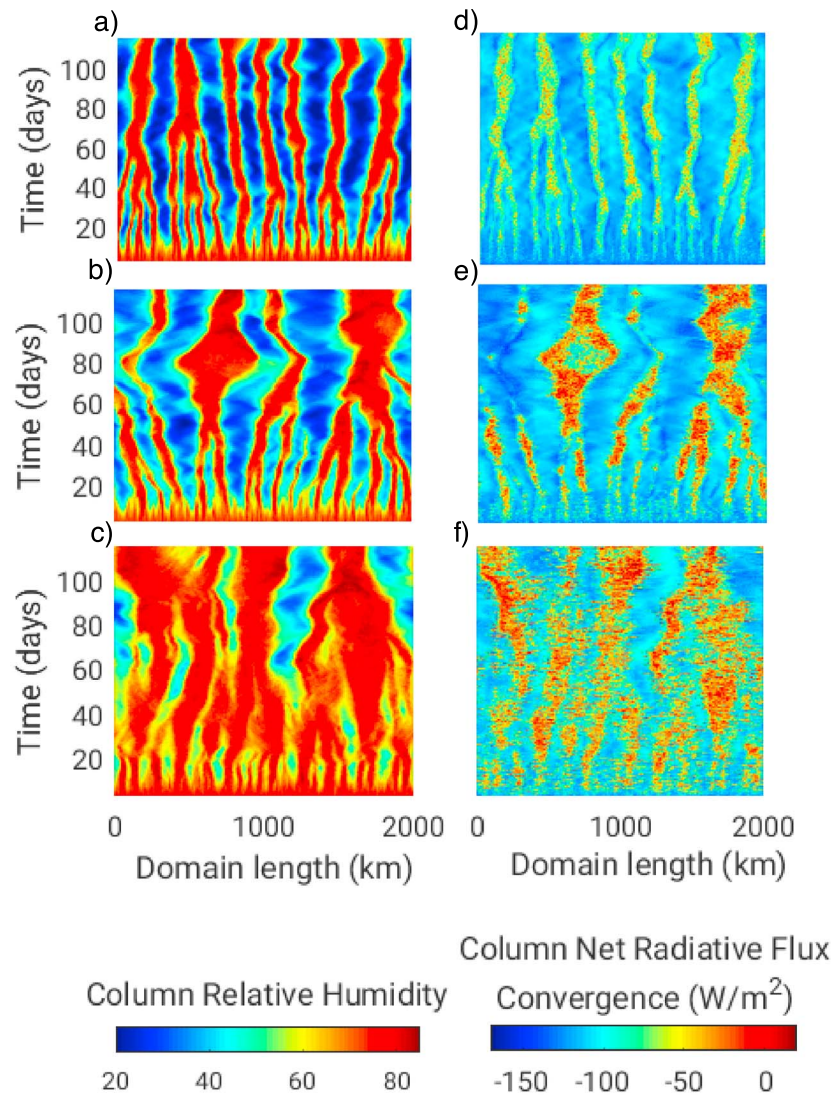
Figure 2. Hovmoller plots of column relative humidity (a–c) and column net radiative flux convergence (d–f). Top plots correspond to simulation "very low," middle plots correspond to simulation "intermediate," and bottom plots correspond to simulation "very high."

domain size sensitivity of RCE in square domains (Muller & Held, 2012), but domain size sensitivity of channel domains has not been established. To address potential concerns of the robustness of our results with respect to domain size, we ran three additional simulations in configurations low, intermediate, and very high on a larger 4,000-km × 120-km domain. As domain size sensitivity is beyond the scope of this paper, we will only refer to the three additional simulations when examining mean properties in the analysis (e.g., mean precipitation) to highlight the key similarities and differences between the different domain sizes in the context of the scientific question being addressed.

4. Overview of the Simulations

In this section we give an overview of the RCE state reached by each of the simulations. Figure 2 shows Hovmoller plots of CRH (a–c) and column net radiative warming (d–f) for three (very low, intermediate, and very high) of the five different CCN concentrations we ran. Figure 2 only show three for brevity, but the trends discussed next are unchanged when considering all five simulations. For these plots, the two variables are computed for each grid cell then averaged in the meridional direction. Evident in Figure 2 is that all simulations self-aggregate into multiple convective clusters. This is consistent with previous studies of

convective self-aggregation in long channel domains, in which convection is not restricted to a single cluster as it does in square domains. However, while all simulations self-aggregate, there are striking differences in the spatial organization of each simulation. Increasing CCN is associated with increased CRH in the dry bands, which implies a lower degree of convective self-aggregation as established by previous studies of convective self-aggregation (summarized in Wing et al., 2017). Looking at the radiation plots, there is increased net column radiative flux convergence in the convective clusters with increasing CCN. This, we will show, can be attributed to increased cloud amount when increasing CCN. When comparing simulations intermediate and very high, it becomes clear that the dry regions experience significant increases in net radiative flux convergence as well, further highlighting the trend of decreased degree of aggregation with increasing CCN. From the perspective of the two-column model presented earlier, it appears there is a systematic reduction in the absolute value of $\widehat{Q}_m$ but no compensating increase in the absolute value of $\widehat{Q}_d$, which would have a negative impact on the surface precipitation as stated in equation (3). More notable differences are the number and size of the convective clusters emerging for each simulation, but this behavior is beyond the scope of this study. From this point onward, we will either deal with domain or block averaged trends. Therefore, our CRH ranked blocks implicitly average out the multiplicity of convective clusters but comprise the behavior of multiple convective systems simultaneously. The last point is, from a statistical standpoint, one of the advantages of a channel domain over a square domain.

Figure 3 shows time series plots of domain mean precipitable water PW (a), domain mean precipitation rate (b), and the domain mean radiative cooling rate (c) for all five simulations of varied CCN concentrations. There is a systematic increase in PW, decrease in precipitation, and decrease in radiative cooling for increasing the CCN concentration. The results of Figures 3a and 3c are consistent with the Hovmoller plots shown previously. Since convectively aggregated systems exhibit lower domain mean water vapor concentrations, higher precipitation rates, and higher radiative cooling rates, the time series plots suggest different degrees of convective aggregation achieved by the simulations. Figures 3a and 3c suggest an equilibrium time scale of around 20–40 days for our simulations, though a good deal of internal variability, especially for the precipitation rates, persists. When a 4-day moving average for the precipitation rates is applied (red lines in Figure 2 b), it becomes clear that simulations very high, high, and intermediate exhibit consistently lower precipitation rates than the two lowest CCN concentration simulations. Simulation low exhibits a consistently lower precipitation rate than simulation very low up until day ~110 where the precipitation rates' internal variability seems to overtake the moving averages of each simulation. However, the simulation timespan is not long enough to establish whether the precipitation rates become systematically indistinguishable. The PW trend is similar in that regard, with consistently increasing PW with increasing CCN except for the two lowest CCN concentrations. The radiative cooling is the most systematic of all three variables, with a consistent decrease with increasing CCN at all times for all simulations.

Table 1 summarizes key variables that quantify the RCE state achieved in each simulation. We average the domain mean surface latent heat flux, $\{LHF\}$; surface sensible latent heat flux, $\{SHF\}$; precipitation rate multiplied by the latent heat of vaporization, $L_v\{P\}$; and the column net radiative flux divergence, $\left\{\widehat{Q}_{net}\right\}$, from day 70 till the end of each simulation. Throughout the paper, $\{\}$ denote a domain mean. We chose day 70 as the starting time for averaging to ensure a statistical equilibrium by the model variables is attained. Unless otherwise stated, all temporal averaging of variables presented in this paper is carried out over this timeframe. The table includes values for the additional larger domain simulations as well. The net energy term is the difference between the radiative cooling and the sum of the sensible and latent heat fluxes. Our simulations achieve a water mass balance, whereby the average latent heat flux is within 1.5 W/m^2 of the precipitation rate for all cases. There is, however, a positive Net energy term with maximum values of 7.6 W/m^2 for the two lowest CCN concentration experiments. The impact of this residual term was found in the upper levels of the domain between 16 and 20 km where there is some warming (1.5 K) over the timeframe of interest. Above 20 km, the Rayleigh damping absorbs whatever remains of the residual warming term. Since the impact of the residual energy term is restricted to upper levels of the domain, we do not think it has an impact on our results.

The results of Table 1 indicate that, on average, there is a systematic reduction in the precipitation, radiative cooling (as already established in Figure 3), and latent heat flux with increasing CCN. The surface sensible heat flux is, as expected, a small contribution to the total surface heat flux in all cases. The mean
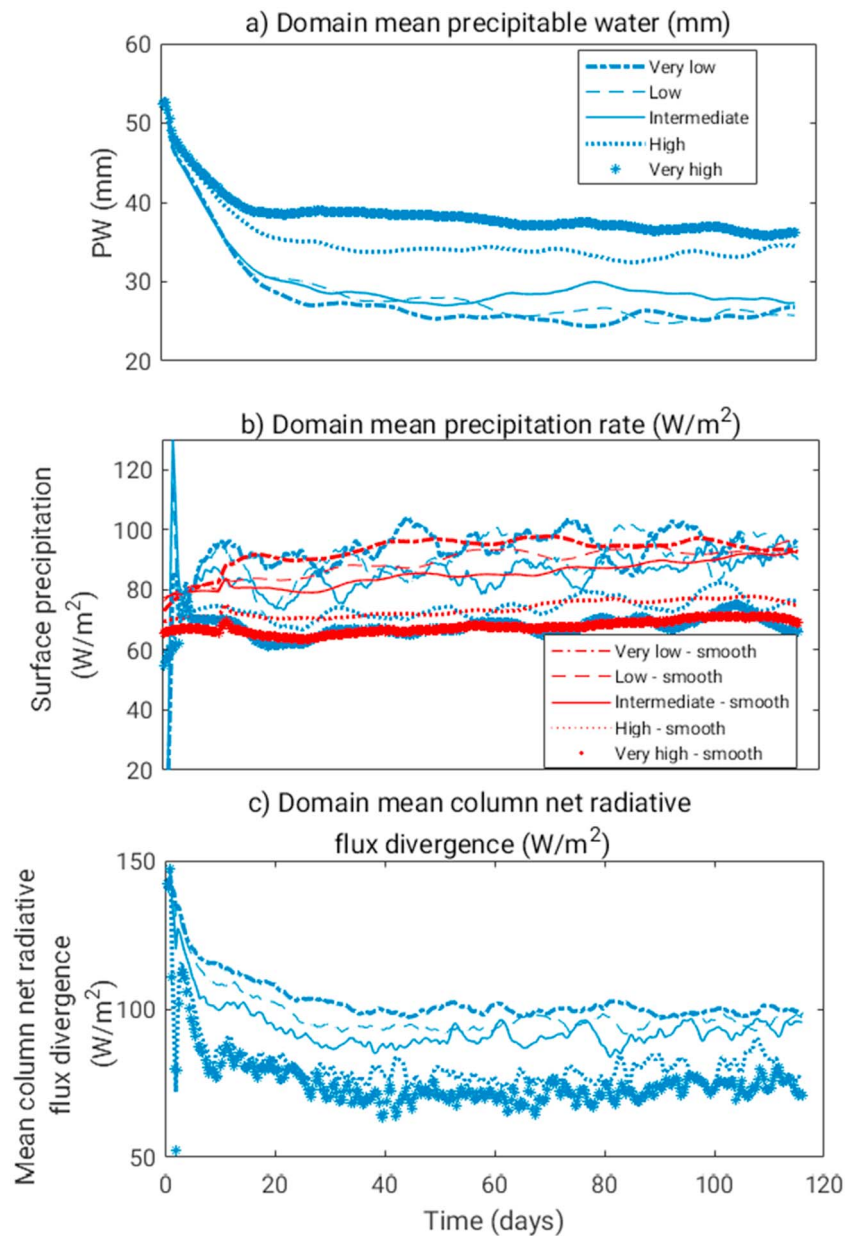
Figure 3. Domain averaged PW (a), precipitation rate (b), and column net radiative flux divergence (c). PW = precipitable water.

precipitation rate's decrease scales with the decrease in radiative cooling, validating that our simulations obey the scaling relation in equation (3). The simulations run on a larger domain exhibit the same trend of decreasing surface and radiative fluxes with increasing CCN. However, for the same CCN concentration, the larger domain simulations have slightly lower energy fluxes. This suggests a weaker degree of self-aggregation for the larger domain simulations, which is contrary to the self-aggregation literature on square domains (Jeevanjee & Romps, 2013; Muller & Held, 2012). For the purposes of sensitivity of the RCE state to the microphysical change of increasing CCN, the differences between the simulations of different domain sizes are smaller than the differences between simulations of different CCN concentrations (e.g., less than 3% reduction in precipitation for doubling the domain size).

Vertical cloud profiles of each simulation are summarized in Figure 4. These profiles are averaged temporally and for all horizontal grid points at each model level. To facilitate comparison, Figure 4a shows the results of simulations very low, low, and intermediate, while Figure 4b shows the results of simulations

Table 1
Summary of Mean Energy Fluxes at Equilibrium Achieved for the Different Simulations

CCN case	$\{LHF\}$ (W/m^2)	$\{SHF\}$ (W/m^2)	$\{P\}$ (W/m^2)	$\left\{\widehat{Q}_{net}\right\}$ (W/m^2)	Net energy (W/m^2)
Very pristine	95.4	11.7	95.4	99.5	7.6
Pristine	91.8	11.7	92.5	95.9	7.6
Intermediate	87.9	11.1	86.4	92.0	7.0
Polluted	76.1	9.2	74.8	80.6	4.7
Very polluted	68.2	7.8	67.8	73.0	2.6
Pristine 2× domain	90.1	11.9	90.6	94.5	7.5
Intermediate 2× domain	85.8	10.5	86.0	88.7	7.6
Very polluted 2× domain	66.8	7.6	67.6	71.1	3.3

Note. CCN = cloud condensation nuclei; *LHF* = latent heat flux; *SHF* = sensible heat flux.

intermediate, high, and very high. We employ this separation in many of our plots. Changes in the cloud and ice profiles are consistent with previous studies of CCN effects on deep convective clouds (e.g., Carrió et al., 2006; Fan et al., 2013, 2016 Kaufman & Koren, 2006; Morrison & Grabowski, 2011; Storer & van den Heever, 2013; Tao et al., 2012), whereby low level clouds decrease (in this case they decrease relative to the total liquid cloud path) at the expense of midlevel clouds and upper level ice clouds. An increase in upper level clouds is consistent with the radiative cooling rate trends we saw in Figures 2 and 3 since the height of these clouds makes them very effective at radiatively warming the upper atmosphere. The increase in high level ice clouds with increasing CCN can be explained by the larger amount of liquid water lofted to the freezing level (the systematic increase in the cloud mixing ratio at around 5 km seen in Figure 4) as well as the smaller mean ice crystal size formed from the freezing of smaller more numerous cloud drops. The former effect increases the total ice amount while the latter effect increases the longevity of ice clouds by decreasing mean ice crystal fall speed. Figure S2 confirms the trend of decreasing ice crystal mean size with increasing CCN.

In order to understand the source of the reduced radiative cooling in our simulations, we list the temporally averaged variables of domain mean net longwave flux divergence, $\left\{\widehat{Q}_{LW}\right\}$; domain mean shortwave flux convergence, $\left\{\widehat{Q}_{SW}\right\}$; clear-sky domain mean net longwave flux divergence, $\left\{\widehat{Q}_{LW,clear}\right\}$; and clear-sky domain mean net shortwave flux convergence, $\left\{\widehat{Q}_{SW,clear}\right\}$, in Table 2. We also list the net radiative cooling terms, $\left\{\widehat{Q}_{net}\right\}$ and $\left\{\widehat{Q}_{net,clear}\right\}$, which correspond to the difference between the respective LW and SW terms. The clear-sky radiation variables are computed online within the Rapid Radiation Transfer Model radiation scheme alongside the cloud inclusive radiation variables. We can see that the reduced radiative cooling with increasing CCN is a result of a simultaneous decrease in $\left\{\widehat{Q}_{LW}\right\}$ and increase in $\left\{\widehat{Q}_{SW}\right\}$, with the former contributing about 75% and the latter 25% to the decreasing trend. By comparing $\left\{\widehat{Q}_{SW}\right\}$ with the clear $\left\{\widehat{Q}_{SW,clear}\right\}$, we can conclude that the SW effect is, on average, a dominantly clear-sky effect. $\left\{\widehat{Q}_{SW}\right\}$ is systematically higher than $\left\{\widehat{Q}_{SW,clear}\right\}$, but the difference never exceeds ~1 W/m^2. This is consistent with the comparisons between clear-sky and cloud inclusive SW warming carried out by Wing and Emanuel (2014), where they found that water vapor modulated SW absorption. Given that water vapor concentrations increase with increasing CCN in our simulations (Figure 3a), it follows that $\left\{\widehat{Q}_{SW}\right\}$ should increase. In comparing $\left\{\widehat{Q}_{LW,clear}\right\}$ with the $\left\{\widehat{Q}_{LW}\right\}$, we can see that the clear-sky term exhibits a small increase with increasing CCN which is contrary to the more substantial decreasing trend the cloud inclusive term exhibits. One way to understand the clear-sky LW trend is to consider the simple three-layer (one surface layer and two atmospheric layers) model presented by Wing and Emanuel (2014). In this model, it is shown that the clear-sky LW radiative flux divergence increases with an increase in the temperature of any of the layers and may increase or decrease with increasing the atmospheric emissivities—changes in which are controlled by changes in the water vapor concentration (at least in the context of the simulations under discussion).
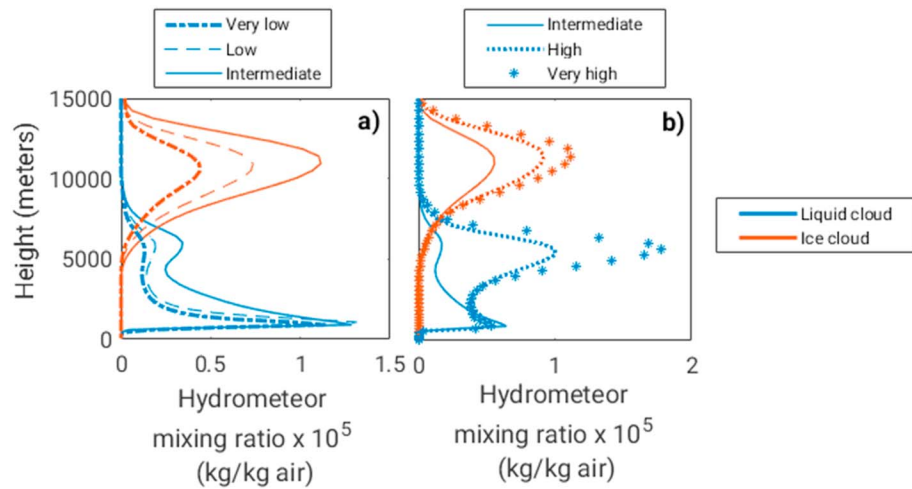
Figure 4. Cloud hydrometeor profiles averaged over entire domain and days 70–116 as a function of height. (a) Low cloud condensation nuclei cases. (b) High cloud condensation nuclei cases.

Therefore, unless one atmospheric layer experiences substantial changes compared to the other atmospheric layer (e.g., an increase in the lower layer water vapor concentration alone would lead to increased LW radiative cooling), no obvious answer to whether an increase or decrease in radiative cooling is incurred when the water vapor concentration increases in both layers. We checked vertical temperature and water vapor concentration profiles and confirmed that with increasing CCN there is a small increase in temperature at upper levels and a simultaneous increase in water vapor at lower and upper levels (Figure S2). Remarkably, the clear-sky radiative cooling $\left\{\widehat{Q}_{net,clear}\right\}$ (final column) suggests that the impacts of the clear-sky SW and clear-sky LW almost cancel out. We can therefore conclude that the increases in LW warming incurred by increases in midlevel and upper level clouds dictate the decreasing radiative cooling trend in our simulations.

Figure 5 shows the distribution of radiative cooling, $\widehat{Q}_{net}$, temporally averaged and plotted against CRH ranked blocks (the second method of block averaging described in the methods section). Figure 5a shows that there is a reduction in radiative cooling in the moist blocks while radiative cooling in the dry blocks is almost unchanged. This validates the observation we made earlier when comparing Figures 2d and 2e. Despite the fact that a decreased radiative cooling in the moist regions of convectively aggregated systems is a positive feedback on convective aggregation (Wing & Emanuel, 2014), there has to be an overcompensating radiative cooling in the dry regions for the overall strength of the convection and thus precipitation to stay the same (equation (3)). Figure 5b shows that with further increasing CCN concentrations the dry regions begin to experience reductions in radiative cooling, which is consistent with the trend of decreasing precipitation we see for these cases. We will explore the repercussions of these changes on the strength of aggregation with further analysis in the next section. To highlight the importance of the cloud radiative effect, we also show the clear-sky radiative cooling rates plotted against CRH ranked blocks. Similar to the cloud inclusive radiative cooling rate, the clear-sky radiative cooling is lower in the moist blocks than in the dry blocks. Therefore, the clear-sky radiative effect contributes to the radiative cooling discrepancy between the moist and dry regions and thus to the aggregation. However, as already highlighted in

Table 2
Clear-Sky and With Cloud Longwave and Shortwave Column Net Radiative Flux Divergences for All Five Cloud Condensation Nuclei Cases

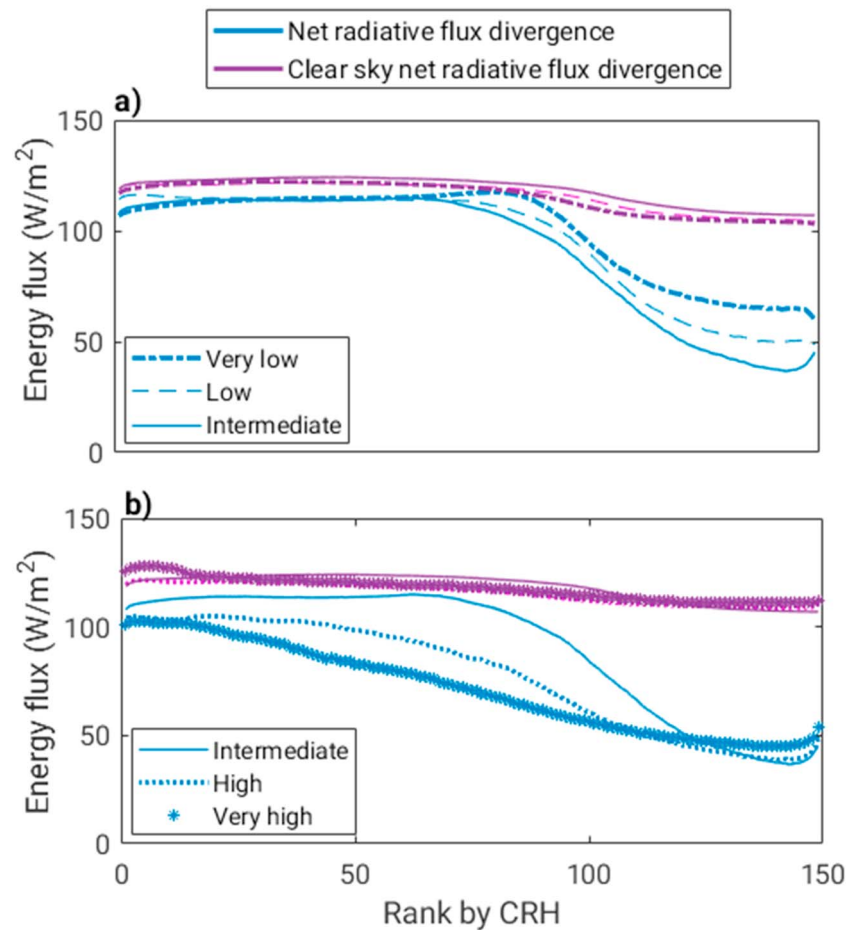| Case	$\left\{\widehat{Q}_{net,LW}\right\}$ (W/m²)	$\left\{\widehat{Q}_{net,SW}\right\}$ (W/m²)	$\left\{\widehat{Q}_{net}\right\}$ (W/m²)	$\left\{\widehat{Q}_{net,LW,clear}\right\}$ (W/m²)	$\left\{\widehat{Q}_{net,SW,clear}\right\}$ (W/m²)	$\left\{\widehat{Q}_{net,clear}\right\}$ (W/m²)
Very low	169.3	69.8	99.5	184.3	69.1	115.2
Low	165.9	70.0	95.9	185.3	69.3	115.9
Intermediate	164.0	72.0	92.0	188.7	70.2	118.5
High	153.7	74.6	79.1	189.8	74.2	115.6
Very high	148.9	76.0	71.8	192.6	74.8	117.7

Figure 5. Surface latent heat flux, column radiative flux divergence, and clear-sky radiative flux divergence against CRH rank. (a) Low cloud condensation nuclei cases and (b) high cloud condensation nuclei cases. CRH = column relative humidity.

Table 2, the net clear-sky term's changes with increasing CCN are barely discernable. Interestingly, the clear-sky rate is still greater than the cloud inclusive rate in the driest blocks (by around 10 W/m^2). This suggests that even at the lowest CCN concentration, there are small amounts of detrained high level clouds throughout the entire dry region. The insensitivity of the clear-sky radiative cooling rate in the dry regions in going from intermediate to high and very high contrasted to the sensitivity of the cloud inclusive radiative cooling rate (Figure 5b) suggests increased detrainment of high level clouds as the source of the reduced radiative cooling in the dry regions. This will be shown visually in section 6.

Before moving on to the next section, we must draw attention to the fact that our self-aggregated simulations exhibit a much stronger sensitivity to the CCN concentration than the previously reported simulations of van den Heever et al. (2011). We think the three leading culprits for this discrepancy are differences in how the simulations were initialized the difference in the dimensionality of the domain used (3-D here vs 2-D in the work of van den Heever et al., 2011), and the difference between how the CCN changes are imposed. Regarding the first point, the simulations of van den Heever et al. (2011) were all initialized with a "control" CCN concentration. Only after the control simulation reached equilibrium was the CCN concentration increased. Hysteresis effects are common in self-aggregated RCE simulations (Wing et al., 2017). For example, simulations that do not achieve self-aggregation (e.g., for reasons such domain size being too small or horizontal resolution being too coarse) retain a self-aggregated state when initialized with an organized PW field. Therefore, it may very well be that the self-aggregated state achieved by a very low CCN concentration in the simulations of van den Heever et al. (2011) was no longer susceptible to changes in that state after the CCN concentration was altered. Regarding the second point, it has been established that 2-D

domains artificially strengthen the regions of subsidence (Stephens et al., 2008; Tompkins, 2000). Since the precipitation response depends on changes in the strength of the overturning circulation (this will be discussed in further detail in a later section of this paper), inflated subsidence can dampen the sensitivity of the self-aggregated state to changes in model physics (such as the CCN concentration in this case). Regarding the third point, the simulations of van den Heever et al. (2011) restricted the CCN increase to an elevated layer between 2 and 4 km while allowing advection to higher model levels. This may have rendered the impact on high level clouds—which in our simulations serve to alter the radiative cooling rates substantially—small.

Other studies that investigated impacts of CCN on RCE are more challenging to compare and reconcile our results with because they dealt with the problem on a different spatial scale. The simulations of Grabowski and Morrison (2011) and Khairoutdinov and Yang (2013), which exhibit a weak sensitivity to CCN, were not designed to incur self-aggregation. Therefore, feedbacks through impacts on the self-aggregated state were not possible. Other possible culprits for the weaker sensitivity are the different microphysics schemes used. Both studies report some reduction in high level ice contrary to the enhancement reported here. Furthermore, Khairoutdinov and Yang (2013) report some enhancement of snow, which points to subtle differences in the microphysics schemes that result in varied partitioning between radiatively active ice and radiatively inactive snow. A more recent study by Seifert et al. (2015) showed an almost complete buffering of the CCN impact on simulations of subsiding RCE (SRCE). Unlike the deep convective organization prevalent in traditional RCE simulations, SRCE deals with a smaller scale radiative-convective equilibrium within the trade wind cumulus system. Therefore, the dynamical feedbacks that arose in SRCE, which acted to buffer the CCN sensitivity, are not applicable here (deepening of the cloud layer with increasing CCN).

While the handful of studies that investigated sensitivity of RCE to CCN saw weak sensitivities, two studies that investigated impacts of microphysical assumptions on RCE found comparable responses to what is reported here. Wu (2002) investigated the sensitivity of RCE to the ice particle fall speed while Grabowski (2003) examined the sensitivity of quasi-RCE in a global aqua planet configuration (with a convective parameterization) to mean cloud particle size. Both these studies found that the configuration with longer lived cloud particles led to atmospheres which were moister, warmer, cloudier, and less precipitating. Given that increasing the CCN concentration in our simulations leads to smaller and longer lived cloud particles in the upper atmosphere, the response of the RCE state we report can be regarded as strikingly similar to the aforementioned studies.

5. MSE Analysis

In this section we employ the MSE budgeting framework developed by Wing and Emanuel (2014) and successfully used in a myriad of studies on convective self-aggregation (e.g., Arnold & Randall, 2015; Becker et al., 2017; Holloway & Woolnough, 2016). Under adiabatic and reversible conditions, the frozen MSE is approximately conserved, rendering it a useful diagnostic in studies of convective aggregation. In this paper, we refer to the frozen MSE as simply the MSE, which is defined as

$$h = c_p T + gz + L_v q_v - L_f q_{ice}, \tag{6}$$

where T is the temperature; z is the height; q_v is the water vapor mixing ratio; q_{ice} is the sum of ice, snow, graupel, and hail mixing ratios; c_p is the specific heat of air; g is the gravitational constant; L_v is the latent heat of vaporization; and L_f is the latent heat of fusion.

For a given block, the time rate of change of the vertically integrated MSE $(\widehat{h})$ is equal to the sum of the surface heat fluxes THF (latent + sensible), column radiative cooling $\widehat{Q}_{net}$ (longwave − shortwave), and horizontal advection $\nabla_h.\widehat{\vec{u}h}$:

$$\frac{\partial \widehat{h}}{\partial t} = -\widehat{Q}_{net} + THF - \nabla_h.\widehat{\vec{u}h}. \tag{7}$$

As in previous studies, the advection term is calculated as a residual term from equation (6). In studies of convective self-aggregation, the useful variable is the square of the column integrated MSE anomaly from

the horizontal mean $\widehat{h}'^2$. Since self-aggregation is characterized by distinctly moist and dry regions, the variance of the column integrated MSE (which is the domain mean of $\widehat{h}'^2$) is a measure of the extent of aggregation. Equation (6) is thus written in terms of $\widehat{h}'^2$ (see Wing and Emanuel, 2014, for a detailed derivation):

$$\frac{1}{2}\frac{\partial \widehat{h}'^2}{\partial t} = -\widehat{Q}_{net}'^{\widehat{h}'} + THF'\widehat{h}' - \widehat{h}' \nabla_h . \widehat{\overrightarrow{u} h}. \tag{8}$$

In self-aggregated convection, moisture is advected from regions of low MSE to high MSE, while sensible heat is advected from high to low MSE. The balance of these terms is typically negative resulting in positive gross moist stability. Some studies report a negative gross moist stability in the initial stages of self-aggregation (e.g., Bretherton et al., 2005). In all cases, we think it is useful to split the advection term into moisture and sensible heat contributions:

$$\widehat{h}' \nabla_h . \widehat{\overrightarrow{u} h} = \widehat{h}' \left(\nabla_h . \overrightarrow{u} \left(L_v q_v - \widehat{L_f q_{ice}} \right) + \nabla_h . \overrightarrow{u} c_p \widehat{T} \right). \tag{9}$$

The terms in equation (9) are also calculated as residual terms from the moisture, hydrometeor, and temperature fields of our output.

Integrating equation (8) with respect to time gives

$$\widehat{h}'^2(block, t) = 2\sum_i \left(\int_0^t x\widehat{h}' \ dt \right) \tag{10}$$

and

$$\left\{ \widehat{h}'^2 \right\}(t) = 2\sum_i \left(\int_0^t \left\{ x\widehat{h}' \right\} dt \right), \tag{11}$$

Where x is each diabatic/adiabatic contribution (i.e., x is equal to $-\widehat{Q}_{net}'$, THF', or $\nabla_h . \widehat{\overrightarrow{u} h}$). Expressions (10) and (11) quantify the individual diabetic and adiabatic contributions to the instantaneous block specific squared MSE anomaly and domain mean MSE variance, respectively.

We are interested in the three-way relationship between CCN concentration, precipitation, and self-aggregation. Thus, we examine how well MSE anomalies translate to precipitation both locally and over the entire domain for all of our simulations. Figure 6a is a scatter plot of block averaged precipitation P plotted against block averaged $\widehat{h}'^2$ for all CCN concentrations. Points shown are from day 70 till the end of each simulation. These are not temporal averages; the values represent the instantaneous values of each variable. The bars represent the standard deviation of the 16 day moving average. Evident in this plot is the correlation between the two variables, and its applicability to any CCN concentration. Since column moisture anomaly dictates column MSE anomaly (due to the weak temperature gradient approximation), Figure 6 a effectively correlates the block specific surface precipitation to column moisture anomaly—a correlation we think is physically sensible. The exception (which is not visible in this plot) is the range of $\widehat{h}'^2$ <0.5 (J/ m^2)^2 and $P < 5$ mm/day, where simulations intermediate, high, and very high precipitate more than the two lowest CCN concentration simulations for the same $\widehat{h}'^2$. This discrepancy represents less than 5% of the total precipitation and is likely due to the different governing dynamics of the shallow convection responsible for precipitation in these lower CRH/$\widehat{h}'^2$ blocks. The correlation explains Figure 6b, in which the temporally averaged self-aggregation metric $\left\{ \widehat{h}'^2 \right\}$ scales with the temporally averaged domain mean precipitation for each simulation (each blue data point corresponds to one of the simulations). $\widehat{h}'^2$ exhibits notable internal variability as alluded to by the scatter bars of both plots (defined here as the standard deviation of the 16-day moving average), but the trend of decreasing $\left\{ \widehat{h}'^2 \right\}$ with decreasing mean precipitation remains discernable. We find this to be a very useful result, because it allows relating the changes in the mean precipitation rate and the local block specific precipitation rates to changes in the diabatic/adiabatic contributions to the growth of MSE anomalies. We also show results from the larger domain simulations
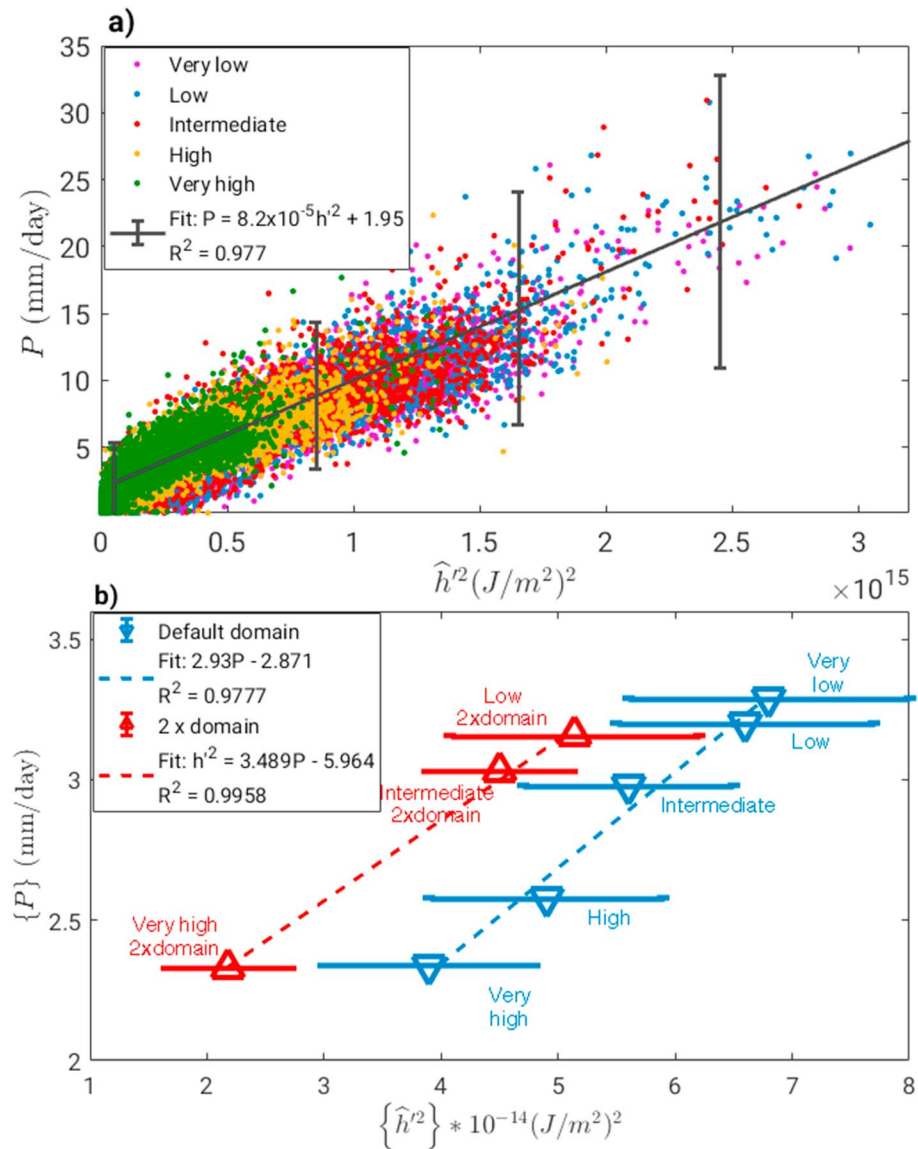
Figure 6. (a) Scatter plot of block specific precipitation versus $\widehat{h'^2}$ for all simulations from day 70 till the end of each simulation. (b) $\left\{\widehat{h'^2}\right\}$ versus mean precipitation rate. Red points represent larger domain simulations.

(red points in Figure 6b). The self-aggregation, as measured by $\left\{\widehat{h'^2}\right\}$, is indeed weaker for the larger domain simulations, but the correlation with mean precipitation remains valid.

Figure 7 shows time series plots of the contribution terms of equation (11) (left), the contributions to the advective term from equation (9) (center), and $\left\{\widehat{h'^2}\right\}$. Top plots are for simulations very low to intermediate, while bottom plots are for intermediate to very high. The sum of the contribution terms in the first panel equates to $\left\{\widehat{h'^2}\right\}$ in the last panel. $\left\{\widehat{h'^2}\right\}$ is plotted as a 16-day moving average (to average out internal variability and facilitate comparison). In Figure 7a, we can see that the radiative contribution increases with increasing CCN, a result consistent with that depicted in Figure 5a. Temporally, the radiative contribution in simulation low overtakes that of very low only after day 70. The trend of increasing radiative contribution is opposite to the trend of decreasing MSE variance, the exception being the first ~70 days of simulation intermediate in which the MSE variance is larger than simulation low (Figure 7c). Since we focus on the final ~50 days, we do not investigate the earlier aggregation of simulation intermediate compared to low,
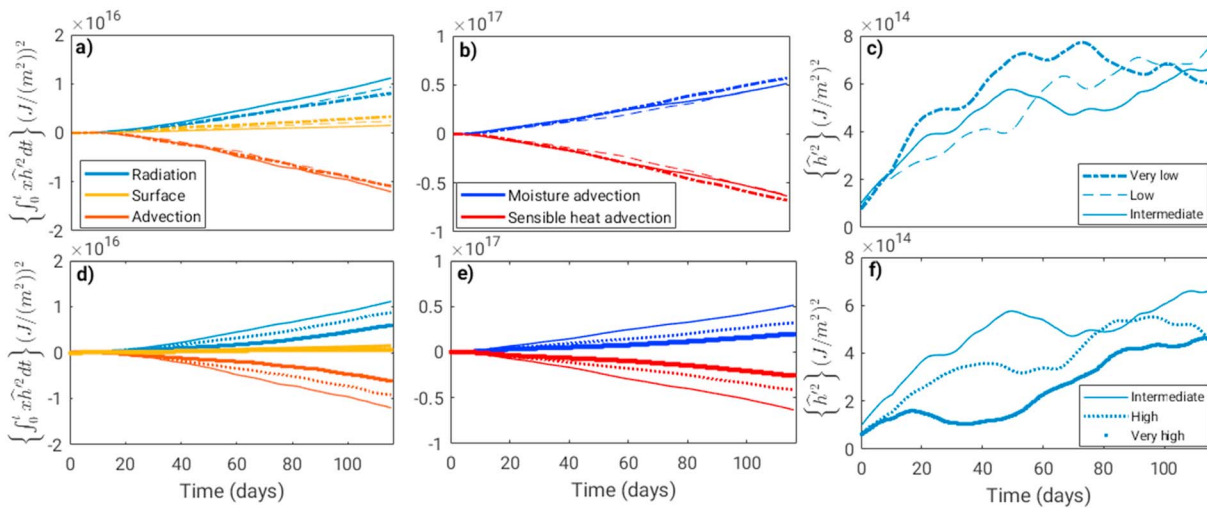
AGU
100
ADVANCING EARTH
AND SPACE SCIENCE

Journal of Advances in Modeling Earth Systems

10.1029/2018MS001523

Figure 7. (left) Diabetic/adiabatic contributions to $\left\{\widehat{h}'^2\right\}$ as function of time. (center) Moisture and sensible heat advective contributions to $\left\{\widehat{h}'^2\right\}$. (right) $\left\{\widehat{h}'^2\right\}$ versus time. Top plots (a–c) depict lower cloud condensation nuclei concentration simulations, while bottom plots (d–f) depict higher cloud condensation nuclei concentrations.

but it seems to stem from former's larger radiative contribution. The decrease in surface contribution with increasing CCN is more systematic throughout the simulations. The advective contribution is virtually indistinguishable for the lowest two CCN cases, but is more negative for the intermediate case. In Figure 7b, we see that simulation very low exhibits both a more positive moisture contribution and a more negative sensible heat contribution from day 70 onward. The other two simulations converge in that timeframe.

Moving on to the higher CCN cases, the trends exhibit a stronger signal. The radiative contribution starts to decrease, indicating that it peaks for simulation intermediate. The surface contribution continues to decrease, though the changes are too small to be discernible in Figure 7d. The advective contribution becomes less negative with increasing CCN, which follows from the weaker circulation of MSE incurred by the weaker radiative contribution. This is highlighted in Figure 7e, where the moisture contribution decreases and the sensible heat contribution becomes less negative.

We interpret the trends in Figure 7 in the following way: the increase in upper level clouds with increasing CCN up until simulation intermediate results in an increase in the radiative contribution to the MSE variance by increasing MSE anomalies in the moist region. This is a positive feedback of increasing CCN on self-aggregation, but it is not manifested in the MSE variance because of the advective and surface contributions which do not conform to the same trend. Their lack of conformity is a result of the changes in the embedded circulations that are not explicit in the MSE variance analysis. Since self-aggregation scales with precipitation in our simulations and the increasing radiative contribution to aggregation is a result of a decrease in the radiative cooling in the moist region without any compensating increase in the dry region (Figure 5a), it follows that the sum of the surface and advective contributions should decrease. In the higher CCN cases, the radiative contribution begins to decrease and this dominates the trend of decreasing MSE variance. Stephens et al. (2008) found that turning off the radiative effects of high level clouds diminished self-aggregation. Our MSE analysis corroborates this result since the radiative contribution to MSE variance is largest for all CCN cases and column radiative cooling anomaly is dictated by radiatively warming clouds (Figure 5).

In Figure 8, we examine the relationship between block specific precipitation (left panel), block specific squared MSE anomaly (center), and the block specific diabatic/adiabatic contributions to $\widehat{h}'^2$ (i.e., equation (9); right). All variables have been temporally averaged. The sum of the contribution terms in right panel equate to $\widehat{h}'^2$ in the center panel. Looking at the first two panels, we can see the correspondence between P and $\widehat{h}'^2$ that was already established in Figure 6. The exception is in blocks ranked <110 for
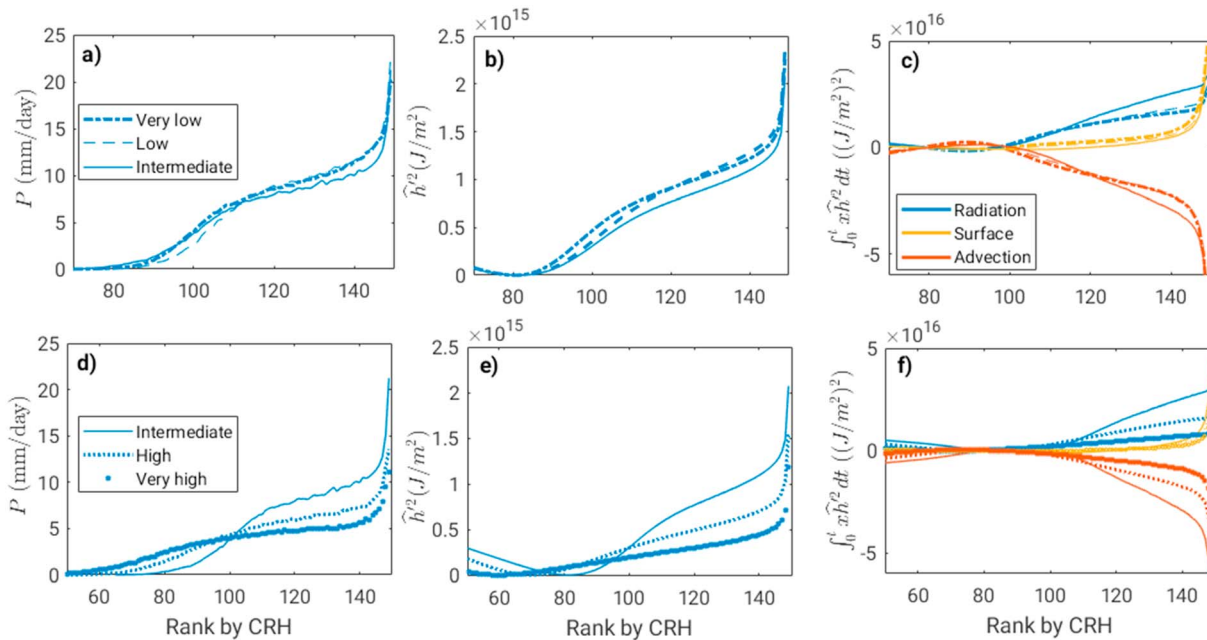
Figure 8. (left) Precipitation rate, P, plotted against CRH rank. (center) $\widehat{h'}^2$ averaged from day 70 till the end of each simulation plotted against the CRH rank. (right) Adiabatic/diabatic contributions to $\widehat{h'}^2$ plotted against CRH rank. Top plots (a–c) depict lower cloud condensation nuclei concentration simulations while bottom plots (d–e) depict higher cloud condensation nuclei concentrations. CRH = column relative humidity.

simulation intermediate whereby the precipitation is higher for the similar $\widehat{h'}^2$ compared to the lower CCN concentrations, a point already mentioned when discussing Figure 6. Simulation low exhibits a similar precipitation rate to simulation very low in the moistest blocks, but lower precipitation rates in the mid-CRH blocks. We see the corresponding reshuffling of $\widehat{h'}^2$ in the center panel, the trend of which is dictated by the radiative contributions shown in the right panel (lower radiative contribution in simulation "pristine" below block ~110 is not visible in Figure 8c due to the scale used). Simulation low thus experiences an increase in the percentage contribution to precipitation by deep convection compared to very low, which is in line with what was found by Storer and van den Heever (2013) for their higher CCN simulations. Increasing the CCN concentration further merely reduces MSE anomalies which reduces precipitation intensity in the moistest blocks (and consequently total precipitation).

6. Circulation Analysis

6.1. Stream Function

Bretherton et al. (2005) introduced a stream function ψ which aids in visualizing the circulation between dry and moist blocks. We compute ψ using the second method of block averaging as we found it shed light on details within the convective core. ψ is given by

$$\psi_i(z) = \psi_{i-1}(z) + \overline{\rho(z)} w_{i-\frac{1}{2}}(z),$$ (12)

where $\overline{\rho(z)}$ is the height dependent density of air, w is the updraft velocity, and i is block CRH rank. $w_{i-\frac{1}{2}}$ is computed as the average of w_i and w_{i-1}. For brevity we only show plots for simulations very low, intermediate, and very high. In Figure 9, contours of ψ are plotted on MSE shading (left panel) and radiative warming shading (center). The right panel is the same as the center panel but zoomed in on the first 2 km. We also show cloud contours in white (dashed lines for ice). ψ values are averaged over days 70–73. The reason we did not average ψ from day 70 till the end of the simulations, as we did in many of other analyses, is to be consistent with averaging timeframes of previous studies utilizing this function. We found that the trends discussed next are insensitive to the averaging timeframe.
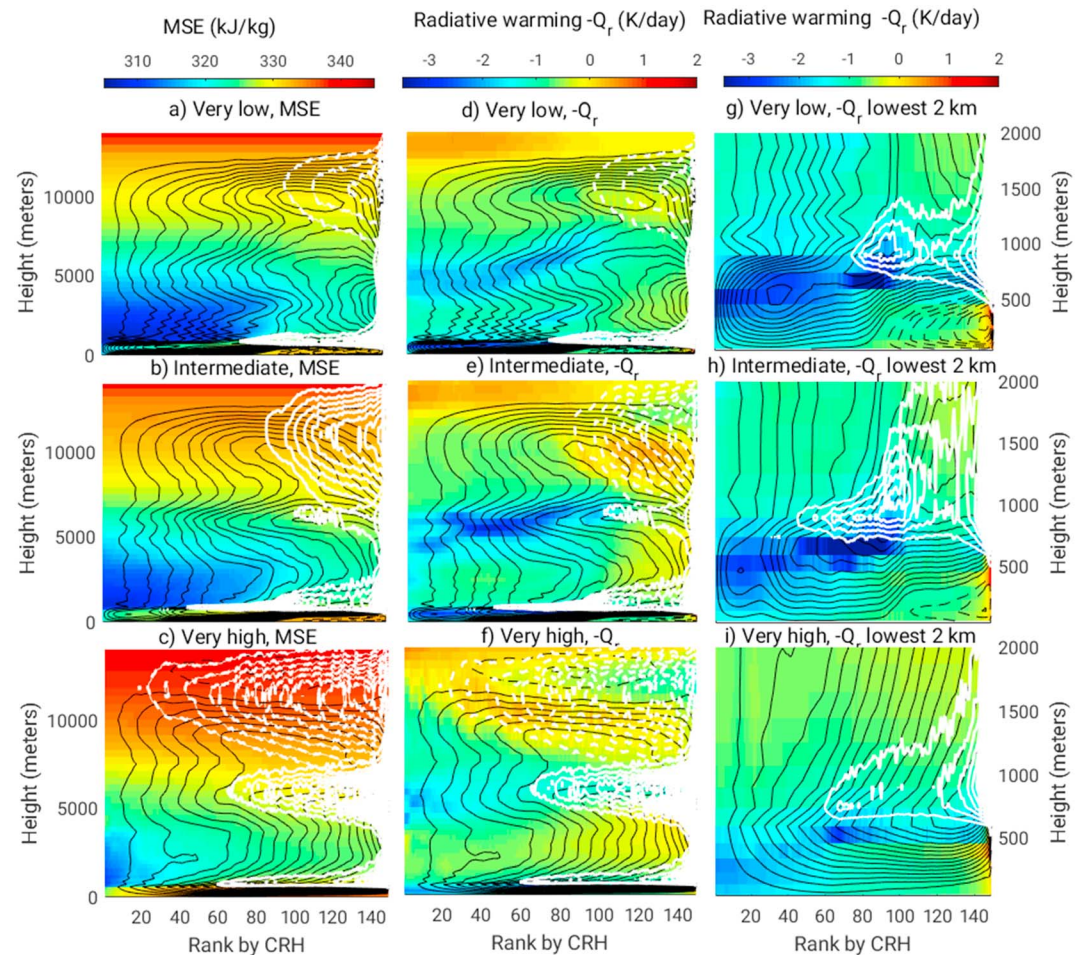
Figure 9. Stream function plots averaged for days 70–73. (top to bottom) Very pristine case (upper), intermediate (center), and very polluted (lower). (left to right) MSE shading (kJ/kg), radiative cooling shading (K/day), and radiative cooling shading (K/day) zoomed in on lowest 2 km. Black solid lines are stream function contours (solid is negative and counterclockwise, dotted is positive and clockwise. Stream lines start at −0.02 kg·m^{-2}·s^{-1} and increase in 0.005 kg·m^{-2}·s^{-1} increments). Solid white lines are liquid cloud contours, dotted white lines are ice cloud contours (from 5×10^{-6} kg/kg air in 5×10^{-6} kg/kg increments). MSE = moist static energy; CRH = column relative humidity.

All three simulations exhibit self-aggregation circulation signatures, namely, the strong midtropospheric radiatively driven subsidence followed by low level subsidence that forces convergence in the driest blocks. However, the extent to which these features manifest varies between simulations. In simulation very low, the signature is most significant. Strong radiative cooling above the moist boundary layer ensures the subsiding stream lines do not return to the moist regions in their dry state. This is a key self-aggregation feedback first described in Muller and Held (2012) and further examined in Muller and Bony (2015). In the boundary layer, the stream lines reconvene in the driest 20 blocks, which aids in remoistening the return flow. Low level clouds seem to drive strong radiative cooling in the mid-CRH blocks while moisture drives it in the driest blocks resulting in two radiative cooling maxima, which may be playing a role in how subsiding air is forced to converge in the driest blocks. Upon return, the flow seems to be interacting with a reverse circulation driven by cold pools (dotted lines in the bottom 500 m). The cold pool circulation has been argued to oppose the main low level circulation in Jeevanjee and Romps (2013), and indeed if the domain size was small enough the cold pool circulation may start to weaken the low level circulation. This does not seem to be the case here; in fact, the cold pool circulation seems to be contributing to the formation of low level clouds by lifting the return flow from block ~80 upward. We did run simulations with the cold pool turned off, but we do not present them here in the interest of brevity. We can confirm that those simulations did not exhibit this reverse circulation and had convective clusters which were smaller in horizontal extent.

Interestingly, they did not exhibit stronger aggregation as measured by MSE variance nor enhanced precipitation. They did show reduced low level cloud amount, lending evidence to the hypothesis that cold pools here contribute to the formation of low level clouds. A final feature of simulation "very pristine" is the seemingly isolated circulation happening around the convective core between the boundary layer and ~5 km. The subject of entrainment in convective self-aggregation has only been recently investigated by Becker et al. (2018), in which it was proposed that the convective cores of self-aggregated systems experience less buoyancy reduction through entrainment by forming a moist shell, whereby the entrained air is recirculated from within the moist region. The circulation referred to here seems to comply with the conditions of a moist shell, rendering it an interesting feature worthy of future investigation.

Moving on to simulation intermediate, we see a similarly strong midlevel subsidence, but an enhanced return of the subsiding air before subsiding deeper into the boundary layer. This can be seen by the decreased density of stream lines in the lower free atmosphere. Radiative cooling decreases in the region just above the boundary layer, which explains the decrease in deeper subsidence. The earlier return flow we see points to a strengthened midlevel circulation, which is consistent with the increase in midlevel clouds. Radiative cooling in the boundary layer remains strong, but the total flow converging in the dry blocks seems to have decreased. We also see a weakened cold pool circulation, which follows from the decreased precipitation. The hypothesized moist shell also seems to be weakened as the midlevel return flow, at around 5 km, is enhanced.

Simulation very high shows remarkable differences from the other two. Midtropospheric and low-level subsidence are weakened, which follows from the decreased radiative cooling rates. There is no convergence of subsiding air in the driest blocks, the stream lines descend impartially into the boundary layer. The cold pool circulation signature disappears. Midlevel clouds increase substantially, which drive strong divergence at midlevels. The mechanism to bring this midlevel outflow down into the boundary layer to be remoistened has weakened, which means the flow must return to the moist region in its dry state. Enhanced midlevel outflow (at around 6–7 km) merely follows from the weakened overturning circulation. Upper level clouds increase in their horizontal extent, decreasing radiative cooling well into the high altitudes of the dry blocks and thus confirming our interpretation of the results in Figure 5b. In the uppermost troposphere, a reverse circulation forms which could promote further cirrus cloud formation. This reverse circulation is reminiscent of the one found in the sensitivity experiment of Bretherton et al. (2005), whereby the autoconversion threshold of ice to snow was increased. Such a microphysical change would have similar repercussion to increasing CCN as both increase the amount of radiatively active ice in the upper atmosphere.

6.2. Quantifying Mean Changes in the Circulation Using the Two-Column Conceptual Model

The stream function in the previous section is a very useful tool for visualizing the circulation and thus qualitatively describe some of its general trends. However, we have not quantified the changes in the state of the circulation. Here we use some of the diagnostics employed in Cronin and Wing (2017) to quantitatively compare our simulations in the context of our simple conceptual model from section 2. In this section, we use the traditional block averaging technique with block sizes of 20 km × 120 km. Instead of focusing on one pressure, such as the 500 hPa, to define the subsidence velocity, we do so for each pressure/height. Hence, for each model level, we compute the temporal average of all subsidence and updraft pressure velocities and refer to them as $\omega_\downarrow$ and $\omega_\uparrow$, respectively. By convention $\omega_\downarrow$ is positive. Continuity dictates that at each model height/pressure:

$$(1-f_h)\omega_\uparrow = -f_h\omega_\downarrow, \tag{13}$$

where f_h is the height dependent subsidence fraction. In self-aggregated convection, f is typically larger than 0.5 throughout the troposphere.

The normalized pressure velocities $f_h\omega_\downarrow$ and $(1 - f_h)\omega_\uparrow$, averaged from day 70 till the end of the simulation, are plotted against height in Figure 10 for all CCN concentrations. When plotted in this fashion, the normalized subsidence and updraft pressure velocities mirror each other. As with all previous results, simulations very low and low show only subtle differences. Simulation low exhibits a slightly elevated low level convergence compared to very low, but the former's updraft/subsidence velocity decreases more with height, indicating higher buoyancy reduction. In the midtroposphere (between 4 and 7 km), simulation low exhibits enhanced pressure velocities. This enhancement indicates a trend of increased strength of the midlevel
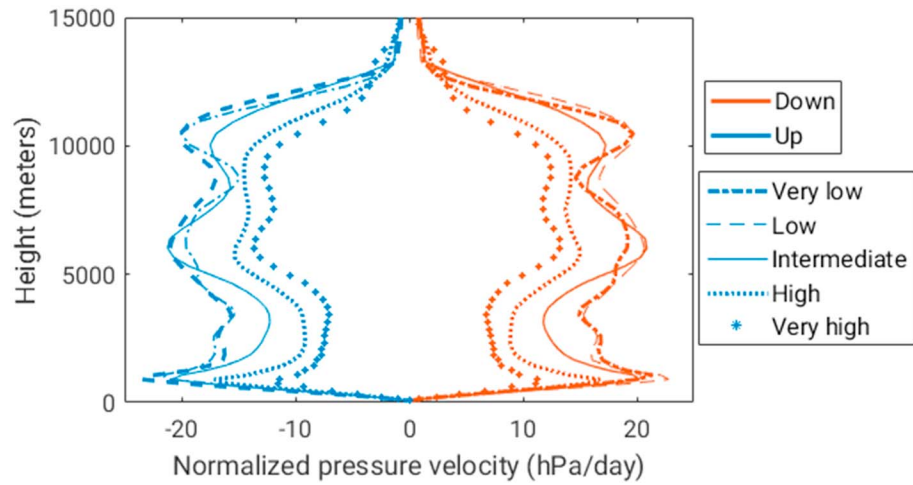
Figure 10. Temporally averaged domain mean area-weighted updraft and subsidence pressure velocities for all cases.

circulation, which does not aid in convective self-aggregation for reasons discussed in the previous subsection. This last point is the reason we became wary of using the 500 hPa pressure level as a reference for comparing the strength of the overturning circulation. Simulation low shows enhanced pressure velocities in the upper troposphere as well, potentially tied to increased high level clouds. Further increasing CCN reduces the pressure velocity throughout the depth of the troposphere. Interestingly, the midlevel circulation stands out when comparing simulation intermediate to low, pointing to its enhanced contribution to the total circulation with increasing CCN.

Three circulations are evident in Figure 10, which challenges the simplified assumption the two-column conceptual model made about one overturning circulation. However, it remains an interesting test to see if an area-weighted radiatively driven pressure velocity correlates with the reduction of precipitation and the weakening of the actual circulation. That is because we understand the crucial role radiative cooling plays in driving subsidence and the thermodynamic constraint on this role expressed in equation (1). For a comparison with the conceptual model we need to derive simulation proxies for the variables of interest to the conceptual model, namely, P, $\widehat{Q}_{net}$, $f\widehat{Q}_d$, $(1-f)\widehat{Q}_m$, and S. $f\omega_{rad}$ can then be calculated using equation (1) with $f\widehat{Q}_d$ in place of $\widehat{Q}_d$. The first two of these variables ($\widehat{Q}_{net}$ and P) are equivalent to the domain mean radiative cooling and precipitation rates $\left\{\widehat{Q}_{net}\right\}$ and $\{P\}$ which have already been computed and listed in Table 1 (though the units of $\left\{\widehat{Q}_{net}\right\}$ and $\{P\}$ are converted to K/day and mm/day, respectively, for this analysis). $\widehat{fQ_d}$ and $\widehat{(1-f)Q_m}$ are the area-weighted dry and moist radiative cooling rates and are calculated in the following way:

$$f\widehat{Q}_d = \frac{1}{M_c}\int_0^{z_{top}}\overline{\rho(z)}f_h(z)\overline{Q_r(\omega_\downarrow>0,z)}\ dz \quad \text{and} \quad \left(1-\widehat{f}\right)Q_m = \frac{1}{M_c}\int_0^{z_{top}}\overline{\rho(z)}(1-f_h(z))\overline{Q_r(\omega_\downarrow<0,z)}\ dz, \quad (14)$$

where $\overline{Q_r(\omega_\downarrow>0,z)}$ and $\overline{Q_r(\omega_\downarrow<0,z)}$ are the radiative cooling rates at height z averaged over the CRH blocks with positive and negative pressure velocities, respectively, and M_c is the reference mass of an air column (kg/m²). z_{top} is taken to be the 300 hPa level. The sum of the two area-weighted radiative cooling rates is $\left\{\widehat{Q}_{net}\right\}$. We note that the area weighting (f or $(1-f)$) is now placed under the ^ since contrary to the conceptual model the subsidence fraction changes with height and is implicitly accounted for in the integration carried out in equation (14). Finally, S is approximated as $\Delta\theta_v/\Delta p$ where the pressure difference is the surface pressure minus 300 hPa and $\Delta\theta_v$ is calculated between the respective pressure levels (Becker et al., 2017). Variables of interest are listed in Table 3 for all CCN cases. We also show the mean subsidence fraction over all heights, $\overline{f}$, to estimate the extent to which the area covered by subsidence changes in our simulations. $\overline{f}$ is 0.6 for the lowest CCN and most aggregated simulation and decreases to 0.5 for the highest CCN and least aggregated simulation. The value of $\overline{f}$ for our most aggregated simulation is in line with the aggregated channel simulations of Cronin and Wing (2017) where the subsidence fraction was found to be ~0.64. The

Table 3
Key Mean Simulation Diagnostics and Metrics

CCN case	$\{P\}$ (mm/day)	$\widehat{fQ_d}$ (K/day)	$\widehat{(1-f)Q_m}$ (K/day)	$\Delta\theta_v$ (K)	$f\omega_{rad}$ (hPa/day)	$\bar{f}$
Very low	3.29	0.82	0.35	30.6	18.8	0.6
Low	3.19	0.83	0.30	31.4	18.6	0.61
Intermediate	2.98	0.81	0.28	33.1	17.1	0.59
High	2.58	0.67	0.26	35.4	13.3	0.56
Very High	2.34	0.55	0.30	36.2	10.6	0.50

Note. The mean precipitation rate (mm/day), the area-weighted dry radiative cooling rate $\widehat{fQ_d}$ (K/day), the area-weighted moist radiative cooling rate $\widehat{(1-f)Q_m}$ (K/day), virtual potential temperature difference $\Delta\theta_v$ (K), the area-weighted radiatively driven subsidence velocity $f\omega_{rad}$ (hPa/day), and the mean subsidence fraction $\bar{f}$. CCN = cloud condensation nuclei.

decrease of $\bar{f}$ with increasing CCN is consistent with our expectation that the subsidence fraction should decrease as self-aggregation weakens. $f_{500\ hPa}$ exhibits the same trend as $\bar{f}$, decreasing from 0.68 to 0.58 from the lowest to the highest CCN concentration.

In Table 3 we can see that $\widehat{fQ_d}$ remains almost unchanged from simulation very low to simulation intermediate then decreases substantially with increasing CCN—a result already hinted to in Figure 5. $\widehat{(1-f)Q_m}$, on the other hand, exhibits a more monotonic decreasing trend with increasing CCN, which is not surprising given that the source of reduced radiative cooling is the high level clouds which originate in the moist region. S increases systematically with increasing CCN, a result we further elucidate in Figure 11a by plotting the mean virtual potential temperature profiles for all simulations. Evident in Figure 11a is the disproportional increase in θ_v in the top of the atmosphere, where high level clouds increase. At the surface, θ_v is dictated by the constant temperature condition, with differences on the order ~1 K due to the elevated moisture concentrations of the higher CCN concentrations. However, higher up in the atmosphere, differences in θ_v increase dramatically. In Figures 11b and 11c, we plot the mean radiative cooling rate (i.e., $\left\{\widehat{Q_{net}}\right\}$ from Table 1) and $f\omega_{rad}$ against precipitation, respectively, to examine the two scaling relations discussed in section 2 simultaneously. We also show results from the larger domain simulations (red triangles). The first scaling (equation (3) and Figure 11b) has already been validated against our simulations in section 4 but is repeated here to help synthesize the simulation results with the conceptual model. First and foremost, we can understand the scaling in Figure 11b as an energy balance: A decrease in mean radiative cooling dictates a decrease in precipitation. However, this result does not explain the mechanism by which this decrease happens. So we turn to the second scaling which proposes that in these aggregated simulations the precipitation decrease can be mechanistically explained by the decrease in the area-weighted radiatively driven subsidence velocity. The central point of the argument made here is that if the subsidence is determined by $\widehat{fQ_d}$ but the high level cloud increase directly affects $\widehat{(1-f)Q_m}$ then the impact on the subsidence is manifested in S. We stress that the second scaling relation is consistent with the well-established thermodynamic constraint on RCE (the first scaling relation) and is merely attempting to connect the energetic constraint to the overturning circulation between the distinct regions of radiatively driven subsidence on the one hand and moist convection on the other. The trend of decreasing $\widehat{fQ_d}$ is contributed to by decreases in both $\bar{f}$ and $\widehat{Q_d}$, but the latter dominates as alluded to by the values of $\widehat{fQ_d}$ and $\bar{f}$ listed in Table 2.

So how does the constraint on subsidence translate to the actual subsidence (shown in Figure 10)? For the high CCN cases (high and very high), the impact of the decreased dry region's radiative cooling rate results in reductions in the strength of all three circulations (Figure 10). On the other hand, cases low and intermediate exhibit less straightforward responses in their circulation as evidenced by Figure 10. We can understand this response by realizing that the enhanced midlevel subsidence for simulations low and intermediate necessitates enhanced midlevel radiative cooling compared to very low. This is further exacerbated by the increased static stability for these two cases (equation (1)). Since the column net radiative cooling $\widehat{(fQ_d)}$ does not increase (Table 3), it follows that low level radiative cooling, which is critical for driving the low level circulation, must decrease. Figure S3 plots the area-weighted dry region's radiative cooling rates against
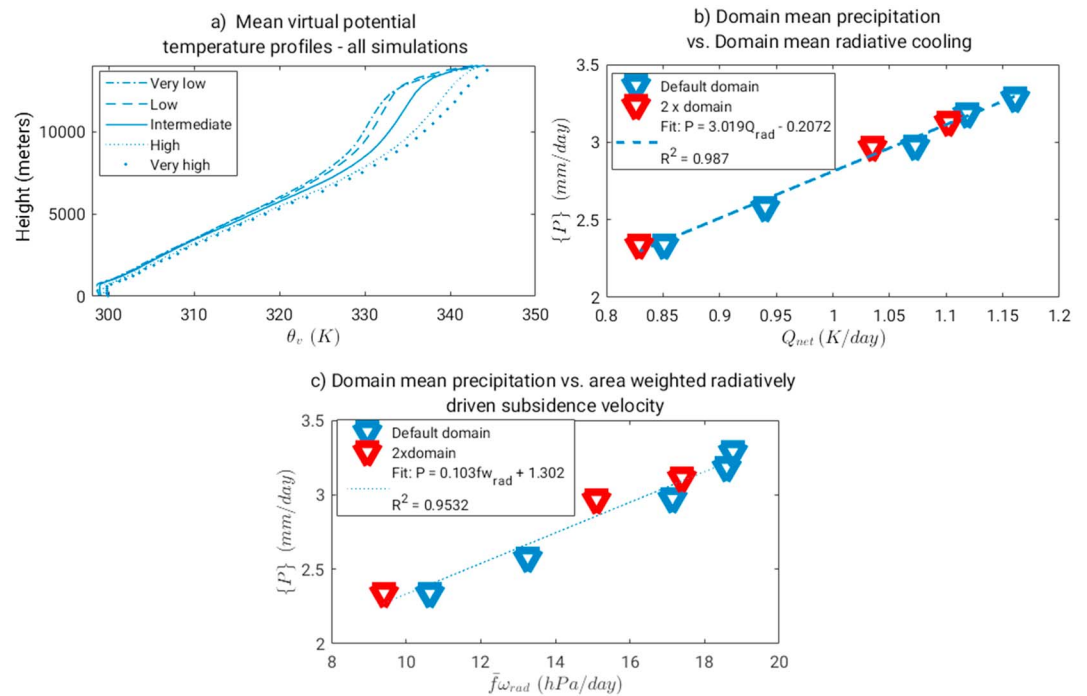
Figure 11. (a) Mean virtual potential temperature profiles against height for all simulations. (b) Mean precipitation plotted against mean radiative cooling rate. (c) Mean precipitation plotted against the area-weighted radiatively driven subsidence velocity.

height and confirms these trends. The low level circulation most closely resembles the singular overturning circulation of the conceptual model since its moisture content is similarly constrained by Clausius-Clapeyron. Therefore, the weakening of the low level circulation can be thought of as the manifestation of the hypothesized reduction in precipitation through the constraint on subsidence (equation (4)).

7. Conclusions

We presented convective self-aggregation simulations in a long channel domain with varied CCN concentrations to investigate the sensitivity of long channel self-aggregated RCE to cloud microphysics. Increasing CCN led to increases in midlevel and upper level clouds, increased PW, decreased precipitation, and decreased radiative cooling. By energy balance, the reduction of precipitation followed from the reduction in radiative cooling which we found was almost exclusively dictated by the increase in upper level cloud amount. We then showed that local and total precipitation correlated with the distribution of MSE anomalies and quantified the radiative, surface, and adiabatic contributions to the domain averaged and CRH-block specific MSE anomalies. We proceeded by investigating changes in the overturning circulation and found three distinct circulations that all underwent changes with increasing CCN, notably a weakening in the low-level circulation at the expense of a more substantial midlevel circulation. We then showed that despite the multifaceted nature of the circulation, changes in the precipitation scaled with changes in the area-weighted radiatively driven subsidence velocity.

Noteworthy similarities exist between this result and what has been reported in the works of Morrison and Grabowski (2011) and Fan et al. (2013). In the former study, an enhanced static stability resulted from increases in high level clouds brought about by increasing the CCN concentration in a simulated ensemble of tropical deep convective clouds. While in the latter, realized simulations over different parts of the globe all saw an increased anvil lifetime due to the lower sedimentation speeds of the smaller ice crystals formed from the smaller cloud droplets associated with a higher CCN concentration.

While our results are coherent and self-consistent, we caution against extrapolating them to a real impact of aerosols on tropical deep convection. We treated the CCN concentration as horizontally and temporally

unchanged, which forces a systematic fingerprint of this microphysical property onto the cloud fields. This is simply not the case in the real tropical atmosphere. Moreover, we intentionally invoked unrealistically high CCN concentrations compared to the tropical maritime atmosphere to induce a strong signal in the self-aggregation response to changes in microphysics. While simulations very low and low may represent a range of realistic CCN concentrations, it is likely that accounting for temporal variability and wet scavenging processes would diminish the CCN impact we can detect when comparing these two simulations. In that regard, we concede that studies which have investigated CCN impacts in more realistic simulations provide more reliable estimates of the cloud and precipitation response to changes in the CCN concentration. Nevertheless, we argue that the study provides three beneficial contributions:

1. The simulations and the two column conceptual they are interpreted with support a thermodynamically constrained impact of aerosol on deep convection. Unlike the process-based reasoning of the aerosol indirect effect, a system-based reasoning actively accounts for the clouds along with the environment they are embedded in. This results in a more robust, albeit idealized, sign of an aerosol impact on deep convection and thus precipitation.
2. The work contributes to mounting evidence that the microphysical pathway of higher CCN concentrations leading to longer lived high level clouds (Fan et al., 2013) is worthy of attention in future modeling and observation studies of aerosol-deep convection interactions.
3. The simulations show a strong sensitivity to how the microphysical scheme partitions the clouds and precipitation (increasing CCN increases cloud amount while decreasing precipitation). This has implications for studies of convective self-aggregation that implicitly employ a variety of one moment and two moment microphysics scheme. While we have not gone about conducting sensitivity simulations of single versus two moment schemes, the sensitivity we found is inherently tied to the microphysical processes that could only be resolved with two moments.

In the spirit of the third contribution, we argue that self-aggregated RCE may be a beneficial test bed for conducting more studies of the role microphysical processes play in their larger scale environment. This framework is particularly beneficial because of the powerful thermodynamic constraints inherent in RCE simulations and the emerging quantitative tools that can be used to analyze them.

References

Albern, N., Voigt, A., Buehler, S. A., & Grützun, V. (2018). Robust and nonrobust impacts of atmospheric cloud-radiative interactions on the tropical circulation and its response to surface warming. *Geophysical Research Letters*, *45*, 8577–8585. https://doi.org/10.1029/2018GL079599

Arnold, N. P., & Randall, D. A. (2015). Global-scale convective aggregation: Implications for the Madden-Julian Oscillation. *Journal of Advances in Modeling Earth Systems*, *7*, 1499–1518. https://doi.org/10.1002/2015MS000498

Becker, T., Bretherton, C. S., Hohenegger, C., & Stevens, B. (2018). Estimating bulk entrainment with unaggregated and aggregated convection. *Geophysical Research Letters*, *45*, 455–462. https://doi.org/10.1002/2017GL076640

Becker, T., Stevens, B., & Hohenegger, C. (2017). Imprint of the convective parameterization and sea-surface temperature on large-scale convective self-aggregation. *Journal of Advances in Modeling Earth Systems*, *9*, 1488–1505. https://doi.org/10.1002/2016MS000865

Boucher, O., Randall, D., Artaxo, P., Bretherton, C., Feingold, G., Forster, P., et al. (2013). Clouds and aerosols. In T. F. Stocker, et al. (Eds.), *Climate change 2013: The physical science basis. Contribution of Working Group I to the Fifth Assessment Report of the Intergovernmental Panel on Climate Change*, (pp. 571–657). Cambridge, United Kingdom and New York, NY, USA: Cambridge University Press.

Bretherton, C. S., Blossey, P. N., & Khairoutdinov, M. (2005). An energy-balance analysis of deep convective self-aggregation above uniform SST. *Journal of the Atmospheric Sciences*, *62*, 4273–4292. https://doi.org/10.1175/JAS3614.1

Carrió, G. G., Prenni, A. J., Cotton, W. R., van den Heever, S. C., & DeMott, P. J. (2006). Impacts of nucleating aerosol on Florida storms. Part I: Mesoscale simulations. *Journal of the Atmospheric Sciences*, *63*, 1752–1775. https://doi.org/10.1175/jas3713.1

Cronin, T. W., & Wing, A. A. (2017). Clouds, circulation, and climate sensitivity in a radiative-convective equilibrium channel model. *Journal of Advances in Modeling Earth Systems*, *9*, 2883–2905. https://doi.org/10.1002/2017MS001111

Dipankar, A., Stevens, B., Heinze, R., Moseley, C., Zängl, G., Giorgetta, M., & Brdar, S. (2015). Large eddy simulation using the general circulation model ICON. *Journal of Advances in Modeling Earth Systems*, *7*, 963–986. https://doi.org/10.1002/2015ms000431

Dunion, J. P. (2011). Rewriting the climatology of the tropical North Atlantic and Caribbean Sea atmosphere. *Journal of Climate*, *24*, 893–908. https://doi.org/10.1175/2010JCLI3496.1

Fan, J., Leung, L. R., Rosenfeld, D., Chen, Q., Li, Z., Zhang, J., & Yan, H. (2013). Microphysical effects determine macrophysical response for aerosol impacts on deep convective clouds. *Proceedings of the National Academy of Sciences*, *110*, E4581–E4590. https://doi.org/10.1073/pnas.1316830110

Fan, J., Wang, Y., Rosenfeld, D., & Liu, X. (2016). Review of aerosol–cloud interactions: Mechanisms, significance, and challenges. *Journal of the Atmospheric Sciences*, *73*, 4221–4252. https://doi.org/10.1175/JAS-D-16-0037.1

Grabowski, W. W. (2003). Impact of cloud microphysics on convective-radiative quasi equilibrium revealed by cloud-resolving convection parameterization. *Journal of Climate*, *16*, 3463–3475. https://doi.org/10.1175/1520-0442(2003)016<3463:IOCMOC>2.0.CO;2

Grabowski, W. W. (2006). Indirect impact of atmospheric aerosols in idealized simulations of convective–radiative quasi equilibrium. *Journal of Climate*, *19*, 4664–4682. https://doi.org/10.1175/JCLI3857.1

Grabowski, W. W., & Morrison, H. (2011). Indirect impact of atmospheric aerosols in idealized simulations of convective-radiative quasi equilibrium. Part II: Double-moment microphysics. *Journal of Climate*, *24*, 1897–1912. https://doi.org/10.1175/2010JCLI3647.1

Hande, L. B., Engler, C., Hoose, C., & Tegen, I. (2016). Parameterizing cloud condensation nuclei concentrations during HOPE. *Atmospheric Chemistry and Physics*, *16*, 12,059–12,079. https://doi.org/10.5194/acp-16-12059-2016

Heinze, R., Dipankar, A., Henken, C. C., Moseley, C., Sourdeval, O., Trömel, S., et al. (2017). Large-eddy simulations over Germany using ICON: A comprehensive evaluation. *Quarterly Journal of the Royal Meteorological Society*, *143*, 69–100. https://doi.org/10.1002/qj.2947

Held, I. M., Hemler, R. S., & Ramaswamy, V. (1993). Radiative-convective equilibrium with explicit two-dimensional moist convection. *Journal of the Atmospheric Sciences*, *50*, 3909–3927. https://doi.org/10.1175/1520-0469(1993)050<3909:RCEWET>2.0.CO;2

Holloway, C. E., Wing, A. A., Bony, S., Muller, C., Masunaga, H., L'Ecuyer, T. S., et al. (2017). Observing convective aggregation. *Surveys in Geophysics*, *38*, 1199–1236. https://doi.org/10.1007/s10712-017-9419-1

Holloway, C. E., & Woolnough, S. J. (2016). The sensitivity of convective aggregation to diabatic processes in idealized radiative-convective equilibrium simulations. *Journal of Advances in Modeling Earth Systems*, *8*, 166–195. https://doi.org/10.1002/2015MS000511

Houze, R. A. Jr. (2004). Mesoscale convective systems. *Reviews of Geophysics*, *42*, RG4003. https://doi.org/10.1029/2004RG000150

Jeevanjee, N., & Romps, D. M. (2013). Convective self-aggregation, cold pools, and domain size. *Geophysical Research Letters*, *40*, 994–998. https://doi.org/10.1002/grl.50204

Kaufman, Y. J., & Koren, I. (2006). Smoke and pollution aerosol effect on cloud cover. *Science*, *313*(5787), 655–658.

Khairoutdinov, M. F., & Yang, C. E. (2013). Cloud-resolving modelling of aerosol indirect effects in idealised radiative-convective equilibrium with interactive and fixed sea surface temperature. *Atmospheric Chemistry and Physics*, *13*, 4133–4144. https://doi.org/10.5194/acp-13-4133-2013

Lilly, D. K. (1962). On the numerical simulation of buoyant convection. *Tellus*, *14*, 148–172. https://doi.org/10.3402/tellusa.v14i2.9537

Manabe, S., & Strickler, R. F. (2002). Thermal equilibrium of the atmosphere with a convective adjustment. *Journal of the Atmospheric Sciences*, *21*, 361–385. https://doi.org/10.1175/1520-0469(1964)021<0361:teotaw>2.0.co;2

Mlawer, E. J., Taubman, S. J., Brown, P. D., Iacono, M. J., & Clough, S. A. (1997). Radiative transfer for inhomogeneous atmospheres: RRTM, a validated correlated-k model for the longwave. *Journal of Geophysical Research*, *102*, 16,663–16,682. https://doi.org/10.1029/97JD00237

Morrison, H., & Grabowski, W. W. (2011). Cloud-system resolving model simulations of aerosol indirect effects on tropical deep convection and its thermodynamic environment. *Atmospheric Chemistry and Physics*, *11*, 10,503–10,523. https://doi.org/10.5194/acp-11-10503-2011

Muller, C., & Bony, S. (2015). What favors convective aggregation and why? *Geophysical Research Letters*, *42*, 5626–5634. https://doi.org/10.1002/2015GL064260

Muller, C. J., & Held, I. M. (2012). Detailed investigation of the self-aggregation of convection in cloud-resolving simulations. *Journal of the Atmospheric Sciences*, *69*, 2551–2565. https://doi.org/10.1175/JAS-D-11-0257.1

Randall, D. (2015). *An introduction to the global circulation of the atmosphere*. Princeton, NJ: Princeton University Press.

Reed, K. A., & Jablonowski, C. (2011). An analytic vortex initialization technique for idealized tropical cyclone studies in AGCMs. *Monthly Weather Review*, *139*(2), 689–710. https://doi.org/10.1175/2010MWR3488.1

Riehl, H., & Malkus, J. S. (1958). On the heat balance in the equatorial trough zone. *Geophysica*, *6*, 503–538.

Seifert, A., & Beheng, K. D. (2006). A two-moment cloud microphysics parameterization for mixed-phase clouds. Part 1: Model description. *Meteorology and Atmospheric Physics*, *92*, 45–66. https://doi.org/10.1007/s00703-005-0112-4

Seifert, A., Heus, T., Pincus, R., & Stevens, B. (2015). Large-eddy simulation of the transient and near-equilibrium behavior of precipitating shallow convection. *Journal of Advances in Modeling Earth Systems*, *7*, 1918–1937. https://doi.org/10.1002/2015MS000489

Sobel, A. H., Nilsson, J., & Polvani, L. M. (2001). The weak temperature gradient approximation and balanced tropical moisture waves*. *Journal of the Atmospheric Sciences*, *58*, 3650–3665. https://doi.org/10.1175/1520-0469(2001)058<3650:TWTGAA>2.0.CO;2

Stein, T. H. M., Holloway, C. E., Tobin, I., & Bony, S. (2017). Observed relationships between cloud vertical structure and convective aggregation over tropical ocean. *Journal of Climate*, *30*, 2187–2207. https://doi.org/10.1175/JCLI-D-16-0125.1

Stephens, G. L., van den Heever, S., & Pakula, L. (2008). Radiative–convective feedbacks in idealized states of radiative–convective equilibrium. *Journal of the Atmospheric Sciences*, *65*, 3899–3916. https://doi.org/10.1175/2008JAS2524.1

Storer, R. L., & van den Heever, S. C. (2013). Microphysical processes evident in aerosol forcing of tropical deep convective clouds. *Journal of the Atmospheric Sciences*, *70*, 430–446. https://doi.org/10.1175/JAS-D-12-076.1

Tao, W. K., Chen, J. P., Li, Z., Wang, C., & Zhang, C. (2012). Impact of aerosols on convective clouds and precipitation. *Reviews of Geophysics*, *50*, RG2001. https://doi.org/10.1029/2011RG000369

Tobin, I., Bony, S., & Roca, R. (2012). Observational evidence for relationships between the degree of aggregation of deep convection, water vapor, surface fluxes, and radiation. *Journal of Climate*, *25*, 6885–6904. https://doi.org/10.1175/JCLI-D-11-00258.1

Tompkins, A. M. (2000). The impact of dimensionality on long-term cloud-resolving model simulations. *Monthly Weather Review*, *128*, 1521–1535. https://doi.org/10.1175/1520-0493(2000)128<1521:TIODOL>2.0.CO;2

Tompkins, B. A. M., & Craig, G. C. (1998). Radiative-convective equilibrium in a three-dimensional cloud-ensemble model. *Quarterly Journal of the Royal Meteorological Society*, *124*, 2073–2097. https://doi.org/10.1002/qj.49712455013

van den Heever, S. C., Stephens, G. L., & Wood, N. B. (2011). Aerosol indirect effects on tropical convection characteristics under conditions of radiative–convective equilibrium. *Journal of the Atmospheric Sciences*, *68*, 699–718. https://doi.org/10.1175/2010JAS3603.1

Wing, A. A., & Cronin, T. W. (2016). Self-aggregation of convection in long channel geometry. *Quarterly Journal of the Royal Meteorological Society*, *142*, 1–15. https://doi.org/10.1002/qj.2628

Wing, A. A., Emanuel, K., Holloway, C. E., & Muller, C. (2017). Convective self-aggregation in numerical simulations: A review. *Surveys in Geophysics*, *38*(6), 1173–1197. https://doi.org/10.1007/s10712-017-9408-4

Wing, A. A., & Emanuel, K. A. (2014). Physical mechanisms controlling self-aggregation of convection in idealized numerical modeling simulations. *Journal of Advances in Modeling Earth Systems*, *6*, 59–74. https://doi.org/10.1002/2013MS000269

Wu, X. (2002). Effects of ice microphysics on tropical radiative-convective-oceanic quasi-equilibrium states. *Journal of the Atmospheric Sciences*, *59*, 1885–1897. https://doi.org/10.1175/1520-0469(2002)059<1885:EOIMOT>2.0.CO;2

Zängl, G., Reinert, D., Rípodas, P., & Baldauf, M. (2015). The ICON (ICOsahedral non-hydrostatic) modelling framework of DWD and MPI-M: Description of the non-hydrostatic dynamical core. *Quarterly Journal of the Royal Meteorological Society*, *141*, 563–579. https://doi.org/10.1002/qj.2378